

Mechanical and Thermal Design of an Optimized PCB Motor for an Integrated Motor Drive System With GaNFETs

Furkan Tokgoz[✉], Student Member, IEEE, Özgür Gülsuna[✉], Furkan Karakaya, Student Member, IEEE, Gokhan Cakal[✉], Student Member, IEEE, and Ozan Keysan[✉], Member, IEEE

Abstract—PCB motors are a viable alternative to commercial electric motors as they are easy to mass-produce and have low manufacturing costs. Moreover, integrated motor drives have gained popularity thanks to their high power density and ease of installation. However, the mechanical and thermal aspects are challenging due to reduced volume. In this paper, a GaNFET switched integrated motor drive axial-flux permanent magnet synchronous machine with a printed circuit board (PCB) stator is designed. The machine is optimized using a multi-objective, non-dominated sorting genetic algorithm (NSGA-II). Two stator types are designed and manufactured to compare the effect of eddy losses. A method for measuring eddy current losses on PCB stators is proposed and used. A mechanical and thermal solution is proposed and tested. Integrated motor drive with sinusoidal pulsed width modulation (SPWM) is used to drive the motor up to 5000 RPM at a 1 MHz switching frequency. The overall system's efficiency is 82% at 0.36 N.m and 90% at 0.18 N.m torque. The system has an output power of 270 W of output power with 59 °C stator temperature that proved the effectiveness of the proposed passive cooling method.

Index Terms—Integrated motor drive, PCB motor, GaNFET, optimization, axial flux.

I. INTRODUCTION

XIAL-FLUX machines with printed circuit board (PCB) stators have advantages over other types of axial-flux machines in terms of manufacturing, construction, and performance [1], [2], [3], [4], [5], [6]. Since the windings are positioned on a printed circuit board, they can be easily mass-produced by highly mature PCB manufacturing industry. The process also assures the high precision of the boards at the micrometer range so that every stator will be identical in terms of electrical properties, isolation, and build quality. Moreover, the cost of each stator board can be reduced by 87% if the number of PCBs is increased from 5 to 1000 pieces [7], [8].

Manuscript received 15 April 2022; revised 17 August 2022; accepted 8 October 2022. Date of publication 12 October 2022; date of current version 21 February 2023. Paper no. TEC-00388-2022. (Corresponding author: Ozan Keysan.)

The authors are with the Electrical-Electronics Engineering, Middle East Technical University, 06800 Ankara, Turkey (e-mail: tokgozfurkan@gmail.com; ozgurgulsuna@gmail.com; kk.frkn@gmail.com; gcakal@metu.edu.tr; keysan@metu.edu.tr).

Color versions of one or more figures in this article are available at <https://doi.org/10.1109/TEC.2022.3213896>.

Digital Object Identifier 10.1109/TEC.2022.3213896

One main challenge of using a PCB stator is that the effective magnetic reluctance will be high since the stator is air-cored, resulting in low phase inductances. Although this can be advantageous in applications that require fast control considering the low electrical time constant, it would also mean that the current ripple will be high for relatively low switching frequencies. The conventional method for overcoming this problem is adding a bulky inductor in series to each phase of the motor [9]. However, this extra inductor will lower both system efficiency and power density.

Another solution to the problem is increasing the switching frequency of the drive. Silicon-based MOSFETs induce high switching losses in increased frequencies. Gallium Nitride (GaN) based switching devices have short turn-on and turn-off times of a few nanoseconds, making them suitable for high switching frequency applications [10]. Since GaNFETs have a small footprint, they are suitable for integrated motor drive systems where the electrical motor and driver are packed into a single housing to have a high power density [11], [12], [13]. However, integrated motor drives have problems in mechanical and thermal aspects as both motor and the driver needs to be cooled from a much smaller surface area [14]. Although [15] offers a thermal solution for single-sided axial-flux machines, the cooling of double-sided machines is not studied in the literature. As both motor and driver are positioned into a single housing, cooling of the heated elements, mechanical rigidity, simplicity, and ease of manufacturing should be considered.

In this paper, an axial-flux permanent magnet synchronous machine with a PCB stator is constructed and coupled with GaNFET switched integrated motor drive with a high switching frequency of 1 MHz. The electric machine is optimized using a multi-objective non-dominated sorting genetic algorithm (NSGA-II) with the developed analytical model. In order to validate the accuracy of the results, finite element analysis (FEA) is completed on ANSYS Maxwell 3D. Two stators with unequal width and constant width radial winding are designed and compared. A novel cooling method is proposed using the PCB stator traces. A mechanical, thermal, and EMI solution for axial-flux double rotor single stator PCB motors is designed, simulated, and implemented in the tightly packed integrated motor drive system. A testing methodology for the eddy current losses on the PCB stator is proposed. The machine is tested

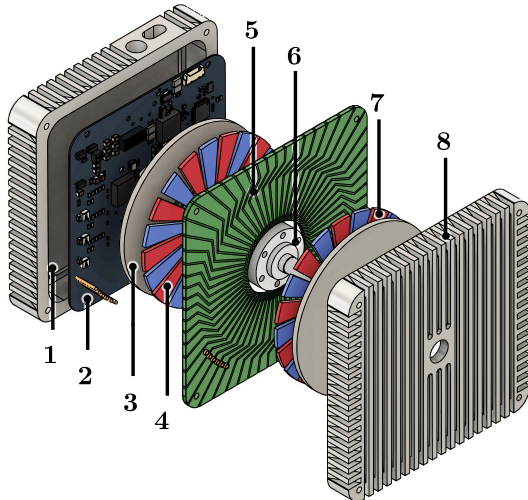


Fig. 1. Exploded view of the designed system. (1) Driver housing, (2) Integrated motor drive board, (3) Rotor back-core, (4) Permanent magnets, (5) PCB stator winding, (6) Shaft, (7) The second rotor, (8) The second housing.

TABLE I
SPECIFICATIONS OF THE INTEGRATED MOTOR DRIVE PCB MOTOR

Rated speed	6000 RPM	Rated frequency	1000 Hz
Rated current	4 A	Rated torque	0.36 N.m
Number of poles	20	Air-gap clearance	1 mm
Magnet thickness	2 mm	Residual flux density	1.38 T
PCB thickness	2 mm	Core thickness	3 mm
Outer diameter	90 mm	Inner diameter	40 mm
PCB trace clearance	0.35 mm	PCB trace width	0.35 mm
PCB number of layers	6	PCB copper thickness	140 μ m
Height	120 mm	Width	120 mm
Motor axial length	35 mm	DC bus voltage	24-48 V

in generating and motoring modes to verify the mechanical, thermal, and electromagnetic results. System Design

The axial-flux permanent magnet machine presented in this paper is in a double-sided rotor single stator configuration as presented in Fig. 1. This configuration offers higher torque and better electrical performance compared to double stator single rotor or single stator single rotor axial flux machines [3]. Some details of the system is introduced at [16]. The system is suitable for industrial products such as robotics and e-mobility applications. The magnets are magnetized in the axial direction. Flux concentration methods such as Halbach array are not preferred in this application to minimize the permanent magnet cost. The stator board is connected to the driver via six pins, two connections for each phase. External housing consists of two parts that serve three purposes: mechanical integration, thermal cooling, and EMI shielding, as explained in the following sections. Overall specifications of the system can be found in Table I.

A. Analytical Calculation and Optimization

The magnetic flux density in the air-gap is modelled to calculate the induced phase voltages and the electromagnetic torque. In this paper, magnetic scalar potential method is used, which was introduced in [17], [18], [19], [20].

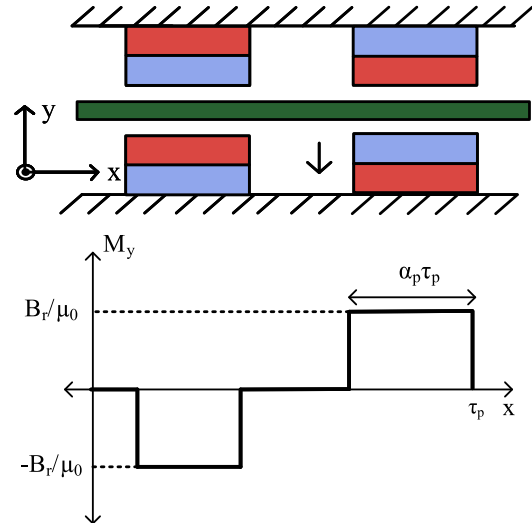


Fig. 2. Radial cross section representation of the machine to represent the magnetic field excitation.

The motor is modeled as presented in Fig. 2 where x-axis is the circumferential direction and y-axis is the axial direction. Note that component sizes are exaggerated for more visibility. It is assumed that the permanent magnets are uniformly magnetized in the y direction and rotor back cores do not saturate, i.e. they have constant permeability. The change of the magnetization vector with respect to angle is given in Fig. 2. The magnetic flux density can be found by the well-known equation

$$\vec{B} = \mu_0 \mu_r \vec{H} + \mu_0 \vec{M} \quad (1)$$

where B , μ_0 , μ_r , H , and M are magnetic flux density, permeability of air, relative permeability of the material, magnetic field intensity, and magnetization vector, respectively. In order to find H , one can use

$$\vec{H} = -\nabla \varphi \quad (2)$$

Magnetic scalar potential φ and magnetization vector M are related with each other as shown in (3).

$$\nabla^2 \varphi = \frac{1}{\mu_r} \nabla \cdot \vec{M} \quad (3)$$

Combining (1), (2), and (3) and the boundary conditions one can find the magnetic flux density in the air-gap as

$$B_y = -\frac{\pi n \mu_0}{\tau_p} \sum_{n=1,2,3...}^{\infty} \left(C_1 e^{\pi ny/\tau_p} - C_2 e^{-\pi ny/\tau_p} \right) \cos \left(\frac{\pi nx}{\tau_p} \right) \quad (4)$$

where n stands for n^{th} order harmonic, τ_p is pole pitch, x is the circumferential position, and y is the axial position. The unknown coefficients, C_1 and C_2 are determined using the boundary conditions.

After calculating the air-gap flux density, one can find the induced phase voltage and electromagnetic torque. Radial winding configuration is used as depicted in Fig. 3, which has 20% less phase resistance to the conventional concentric winding [7]. Radial winding has a better total harmonic distortion (THD) in induced phase voltage compared to other winding types which is

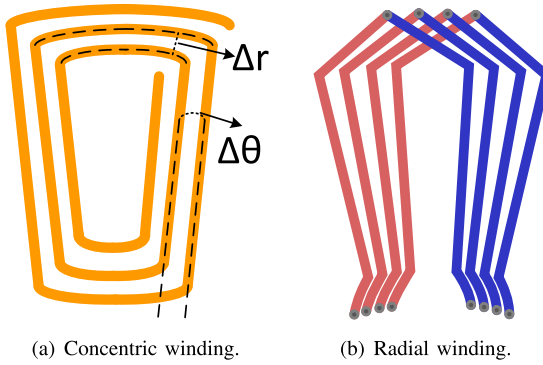


Fig. 3. Concentric and radial winding configurations for the PCB motor.

beneficial in high fundamental frequency application that is used in this paper. The induced phase voltage and the electromagnetic torque is calculated by finding the parameters of Δr and $\Delta\theta$ as shown in Fig. 3, which are variations in radius and angle between each adjacent copper traces.

After finding the flux linkage created by each loop of the winding, one can find the induced phase voltage of the winding as shown in (5).

$$E_a = 2\pi\sqrt{2} f \lambda_{pp} c k_d \quad (5)$$

where E_a is the induced phase voltage, f is the fundamental frequency, λ_{pp} is the total flux linkage of one phase of the winding, c is the number of concentric coils connected in series, k_d is the distribution factor of the winding. Next, electromagnetic torque is found using flux linkage and the current passing through coils as shown in (6).

$$T = \frac{3\sqrt{2}}{4} I_a \lambda_{pp} c p k_d \quad (6)$$

where T is the electromagnetic torque, I_a is the current, p is the pole number of the motor. Using constructed analytical model, a multi-objective genetic optimization algorithm is run using NSGA-II [21]. NSGA-II optimization algorithm offers fast convergence for multi objective optimization with several design variables [22]. The efficiency of the motor and the power density (kW/l) are chosen as two objective functions of the optimization algorithm.

Next, inputs of the optimization algorithm and design parameters are chosen. Since the cost function is analytical in this case, the evaluation of each cost function takes around 0.02 seconds so that the number of design parameters can be increased. The design parameters of the optimization algorithm are chosen as the phase current, the thickness of the copper traces of the PCB, number of turns of each coil, the thickness of the magnets, number of poles, the outer diameter of the motor, and the inner diameter of the motor.

The generation and population sizes are chosen as 100. The resultant Pareto frontier can be seen in Fig. 4. The blue dot in Fig. 4 is the chosen as the optimum design as it has high power density without sacrificing efficiency. The parameters of the design is given in Table I.

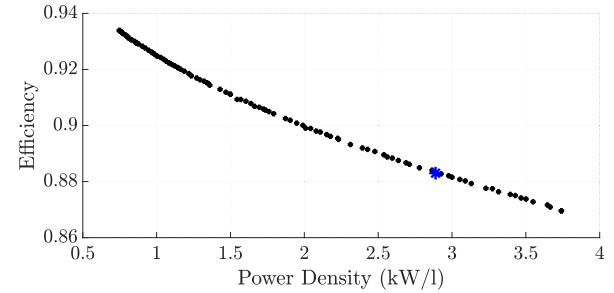


Fig. 4. Multi-objective optimization of AFPMSM using developed analytical model. Blue dot is the prototype.

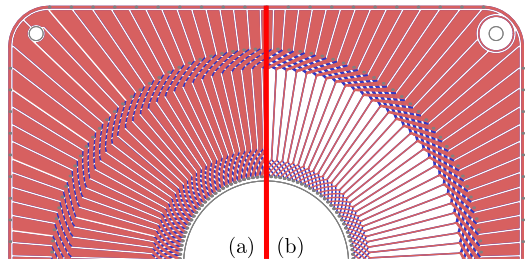


Fig. 5. (a) Stator with unequal width trace. (b) Stator with 0.35 mm width trace.

B. Electromagnetic Design and Effect of Trace Width

After getting necessary parameters from optimization results, such as magnet thickness, inner and outer diameters, number of turns, number of poles, width of the copper traces, and the phase current, one can build the electromagnetic model.

There are various stator windings for PCB motors that is already investigated in [7]. The radial winding, which is the winding type that is used in this paper, has the highest induced voltage and torque value while having 24% less phase resistance than the concentric winding. Unequal width copper trace technique is used in order to reduce the phase resistance of the winding by better utilizing the surface area of the PCB. As the radius of the copper trace increases, the distance between two adjacent traces also increases. The main advantage of using unequal width trace is that the phase resistance of the windings is lower compared to constant width trace since copper cross-section area is higher. Increasing the total copper area also decreases the thermal stress since it offers a lower thermal resistance. However, increasing the copper trace width also results in increase in eddy current losses, especially in a machine where fundamental frequency is 1 kHz. For that purpose, two different winding designs have been done to compare the unequal width winding's advantages and disadvantages over constant width winding. The designed stator windings can be seen in Fig. 5. The stator is manufactured from outside of standard PCB manufacturing ranges in order to increase the copper fill factor. The cost of the PCB increases as the specifications of the board changes. At high volume production the cost of tooling will be minimal since the base cost of the tooling for the PCB manufacturing equipment will be divided by the number of manufactured stator. The minimum

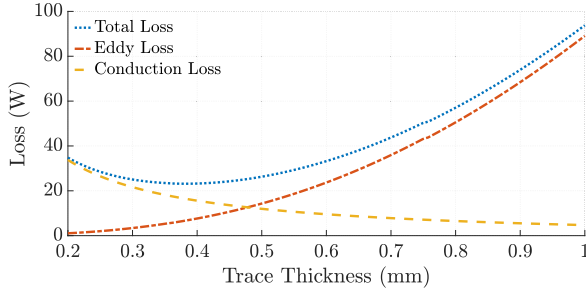


Fig. 6. Change of eddy losses and conduction losses with respect to copper trace width.

clearance between PCB traces are specified by the IPC2211 standard.

Steinmetz equation is used for analytical estimation of eddy current loss of the PCB windings

$$P_{eddy} = B_{peak}^2 f^2 \sigma w_{cu}^2 V_{copper} \quad (7)$$

where P_{eddy} is the total power loss of eddy currents, i is the order of harmonics, B_{peak} is the peak of each harmonic of the magnetic flux density, f is the fundamental frequency, σ is the conductivity of the copper, w_{cu} is the copper trace width, and V_{copper} is the total copper volume inside of the stator. Since there are harmonics in the air-gap flux density, the effect of each harmonic of air-gap flux density to the eddy losses by including the peak of magnetic flux density for every harmonic order in (8).

$$P_{eddy} = \sum_{i=1}^h B_{peak}(i)^2 (i f)^2 \sigma w_{cu}^2 V_{copper} \quad (8)$$

The eddy losses are estimated to be on the width of the trace as presented in Fig. 7. Note that, the mean trace width is calculated for the unequal width winding. The optimum trace width for the constant width stator is chosen by comparing the conduction losses with the eddy current losses on the stator windings. The comparison of the losses at 1 kHz rated frequency and rated current is presented in Fig. 6. As can be seen from the figure, the total losses is minimum at around 0.35 mm trace width. As the trace width is further increased the eddy losses become significant. If the trace width decreased, conduction losses will increase as the cross section area is reduced. Analytical results show that eddy current loss on 0.35 mm trace width winding is 5 W whereas the losses of the unequal width winding is 52 W.

In this paper ANSYS Maxwell 3D is used for electromagnetic FEA. Induced eddy current in single trace of each winding is presented in Fig. 7. Total eddy current power loss of the unequal width winding is found as 66 W in FEA whereas the eddy current loss of the stator with 0.35 mm trace width is 5.9 W. FEA results of both of the windings are presented in Table II.

The results show that while the DC resistance of the unequal width winding is 40% lower than constant width winding, it is not a feasible solution for high speed applications as in this study since the fundamental frequency is high that results in high eddy current loss on copper traces. However, it is a good solution to

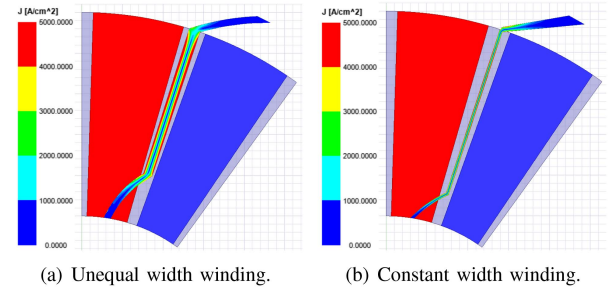


Fig. 7. Induced eddy current densities for two winding configurations at 6000 RPM.

TABLE II
FEA RESULTS OF TWO STATORS

Parameter	Constant 0.35 mm Width	Unequal Width
Phase Resistance	0.36 Ω	0.17 Ω
Copper Loss	17.3 W	8.3 W
Eddy Loss	5.9 W	66 W



Fig. 8. Integrated GaN switched motor driver of the system. (a) Front face of the driver board. (b) Back face of the driver board.

reduce the copper losses on the stator for applications that does not have high fundamental frequency.

C. Motor Drive Design

The predominant disadvantage of an air-cored motor is its relatively low inductance. Low phase inductance results in large torque and current ripple, which can even exceed the current limits of the switches, thus causing failure [23]. The most apparent solution is connecting a series inductor to the motor phases. Then again extra inductor also produces heat, reducing system efficiency while increasing the weight, volume, and cost. Increasing the switching frequency is an alternative solution that comes with increased switching losses, but wide-bandgap devices showed that loss produced at high frequencies is minimal with this technology.

The power electronic converter and its designated controller, namely the power stage and control stage, are combined on a single board that can fit inside of the housing. The designed driver board and the block diagram of the integrated motor drive are presented in Fig. 8 and 9. The drive system is designed such that the input voltage ranges between 24–48 V, and the current capability is 4 A_{rms} at a rated electrical frequency of 1000 Hz.

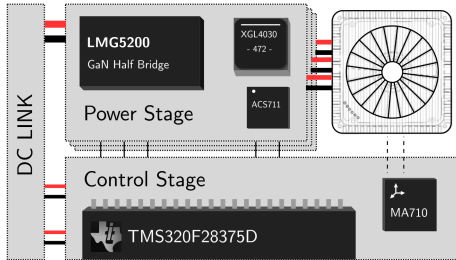


Fig. 9. System depiction for the electronics including the MCU, inverter leg and sensors.

The power stage comprises monolithic GaNFET switches with integrated gate drivers, namely LMG5200, powder-cored power inductors (XGL4030-472), and hall effect type current sensors. The stator design revealed a phase inductance of $3.1 \mu\text{H}$ with the combination of phase filter inductor, total inductance per phase becomes $6.1 \mu\text{H}$. The switching frequency is varied between 500 kHz to 2 MHz to observe its effect. The simulation and resistive-inductive load tests show that the current ripple is 1.3 A at 1 MHz switching frequency.

The control stage is composed of hall effect type encoder, communication interfaces, converters, regulators, and a microcontroller unit (MCU). The selected microcontroller (TMS320F28375D) is 32 b, dual-core, which operates at 200 MHz.

The field-oriented control scheme is implemented with the sinusoidal pulse-width modulation (SPWM) scheme. PI controller for the current loops with feed-forward compensation runs at 100 kHz. The control algorithm and the modulation selection is not optimized but chosen solely to verify the designed system.

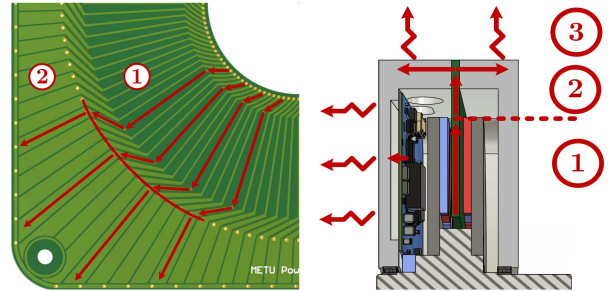
D. Mechanical and Thermal Design

The inherently flat shape of conventional PCBs with the combination of dimensions and the power density criteria, the form becomes square and pancake-like, as presented in Fig. 1.

The rotor consists of two back-cores, which the magnets are glued on, and they are connected with a shaft made out of 7075 alloy of aluminum with the weight considerations in mind. Mechanical stresses on the rotor are concentrated on the boundaries between permanent magnets and steel back-core. Stress analysis showed that the resultant shear stress is around 0.32 MPa in the radial direction, which is just 5% of the 6.8 MPa strength of epoxy glue.

The rotor with the shaft is supported through the bearings, while the stator PCB is supported from its circumference. The outer edges of the stator serve two purposes. The fundamental one is for mechanical support, while the second is to dissipate the heat generated in the stator. The PCB is square shaped, and the area between the outline and circular windings is used to install extra copper traces to conduct heat more effectively, as shown in Fig. 10.

The case is the main construct, and it holds different parts together while protecting them from environmental conditions. It has the same smoothed-square shape as the stator PCB with



(a) Heat flow at the quarter of the stator board.
(b) Heat flow of the stator and driver board.

Fig. 10. Heat flow path of the integrated motor drive. (1) Heat generation inside of the electrically active part, (2) The heat conduction through the electrically inactive parts of the stator, (3) Natural heat convection path to the ambient through the fins of housing body.

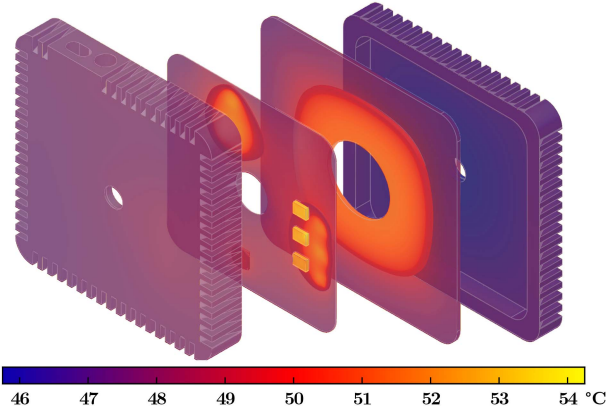


Fig. 11. Thermal simulation results of the model under full load.

an extruded profile. The integration of the shaft with the case is important since the air gap depends on both parts.

There are several considerations to be taken to keep the operating temperature under control. The first of the two main heat sources in the system is stator PCB. As mentioned above, there are heat transfer traces on the outer edges of the windings, and they are thermally connected to the casing, which naturally the heat flows to the ambient. The interface between the stator and the housing is important to increase the heat transfer rate; therefore, thermal pads are placed. The heat loss in the driver board is the second heat source. GaN switches, microcontroller, and the output filters are placed on the bottom of the PCB, directly contacting the casing to maximize heat dissipation. Fins are engraved to increase the surface area of the housing and to reduce thermal resistance.

A thermal FEA model is built to estimate the temperatures of the components with total loss of 23 W for the stator board and 10.9 W for the driver board are injected as the heat source. An air convection rate of $12 \text{ W/m}^2 \cdot \text{K}$ is used outside the housings at an ambient air temperature of 25°C . The results of the simulation are presented in Fig. 11. The temperature of the housings reached 46°C , the inner diameter of the stator reached 52°C and the surface of the GaN switches reached 54°C which is a safe value for operation. It can also be stated that the output power is not



Fig. 12. Enclosed integrated motor drive system connected to the load.

limited by the thermal stresses, but rather limited by the current and voltage ratings for the switches.

II. IMPLEMENTATION

In order to test proposed topology, a prototype is constructed. Unequal width and constant width stators are manufactured. Both boards have six layers, with each layer $140\ \mu\text{m}$ copper thickness. The total thickness of the PCB is 2 mm. The manufactured stators are presented in Fig. 5.

The machine's rotors are constructed using S235 grade steel, which has a low percentage of carbon to improve the magnetic properties. The thickness of the rotor back cores is 3 mm. N48H graded NdFeB permanent magnets with 2 mm thickness are used on the rotor. The rare-earth magnet is chosen for this applications to increase the magnetic loading of the air-cored machine. Ferrite magnets are not considered as they have lower remanence flux density compared to NdFeB magnets [24]. There are no slots for permanent magnets on rotor back cores to reduce the leakage flux around the magnets.

The machine is assembled, and thermal interface material is placed between housings and the stator face to reduce the thermal resistance in between. The complete setup can be seen in Fig. 12. Overall weight of the machine of is measured to be 1067 g.

A. Open Circuit Tests

Comparing induced phase voltages of FEA and test results is one of the easiest ways to validate the design's accuracy. The test setup in Fig. 13 has been used for the open-circuit test. A prime mover is mechanically coupled to the shaft of the PCB motor, and the motor is rotated at various speeds. The resultant three-phase open circuit voltage waveform can be seen in Fig. 14. A comparison of the RMS of the phase voltages of FEA and test results can be seen in Fig. 15. Test results are in good agreement with each other, which proves the validity of the design.

B. Estimation of Mechanical and Eddy Losses

A testing methodology is proposed to determine all loss components such as Coulomb, viscous, windage, and eddy current losses on stators. As these losses change with varying

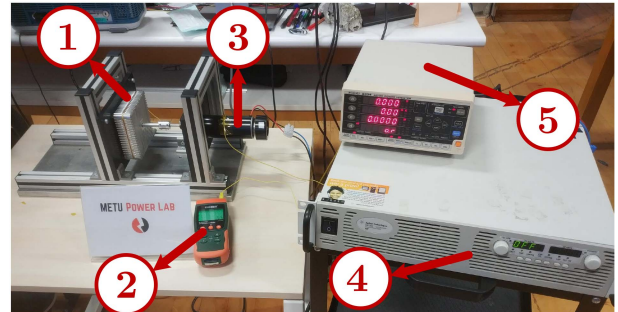


Fig. 13. Test setup for open circuit test and the estimation of mechanical and eddy losses. (1) AFPMMSM with different stators, (2) Temperature logger, (3) DC motor, (4) DC supply, (5) DC wattmeter.

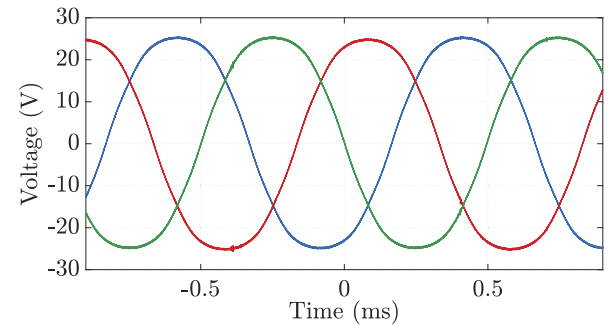


Fig. 14. Open circuit induced phase voltages at 6000 RPM.

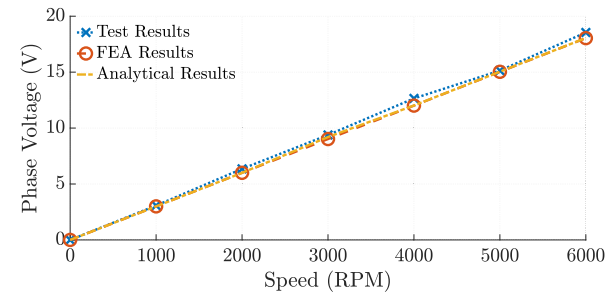


Fig. 15. Variation of open circuit induced phase voltages with rotational speed.

rotational speeds, separating the mechanical and eddy losses from each other can be challenging. A dummy board with the exact dimensions of the actual stator is 3D printed as presented in Fig. 16. Since the material used in the 3D printing process, polylactic acid (PLA), is not electrically conductive, there will be no eddy current induced on the stator. So, one can estimate the mechanical losses using the dummy stator.

The testing methodology is as follows:

- Rotate the prime mover at different speeds starting from 1000 RPM to 6000 RPM until it reaches thermal steady-state. Record the input voltage, current, and temperature of the mover.
- Repeat the first step with PCB the motor with the dummy stator mechanically coupled and record the same measurements for the same speeds and temperatures. Estimate the mechanical and windage power losses from the difference between input powers of the first two cases.



(a) 3D printed dummy stator board. (b) PCB stator board.

Fig. 16. Stator boards for measurement of mechanical eddy current losses.

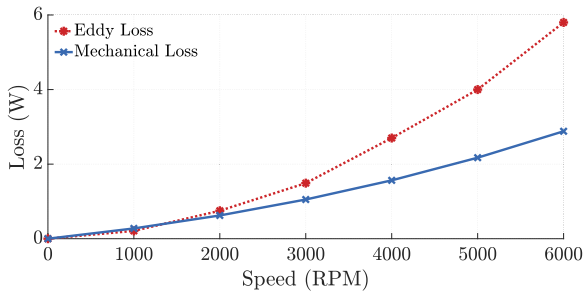


Fig. 17. Mechanical and eddy losses of the system with respect to rotational speed.

TABLE III
EDDY CURRENT LOSS OF THE SYSTEM AT 6000 RPM

Winding type	Analytical	FEA	Test
0.35 mm width	5 W	5.9 W	5.8 W
Unequal width	52 W	66 W	62 W

- Replace the dummy stator with the actual PCB stator. Repeat the test for the same speed and temperature values. The difference between the dummy stator and the PCB stator will be equal to eddy current loss in copper traces. After recording the measurements of the input powers using a power analyzer, the mechanical power loss can be curve fitted to the following equation

$$P_m = k_C w + k_V w^2 + k_W w^3 \quad (9)$$

where k_C , k_V , and k_W constants for Coulomb, viscous, and windage torque. P_m is the mechanical loss and w is the rotational speed in rad/s . The resultant mechanical and the eddy current losses of the system is found as shown in Fig. 17. The mechanical losses in the system is more dominant at lower rotational speeds. However as the speed is increased eddy losses increases parabolically which becomes the major limitation higher speeds. The winding needs to be carefully designed at higher operating speeds.

A comparison of the eddy current losses of the analytical model, FEA simulations, and test results are presented in Table III. The eddy losses of this high fundamental frequency

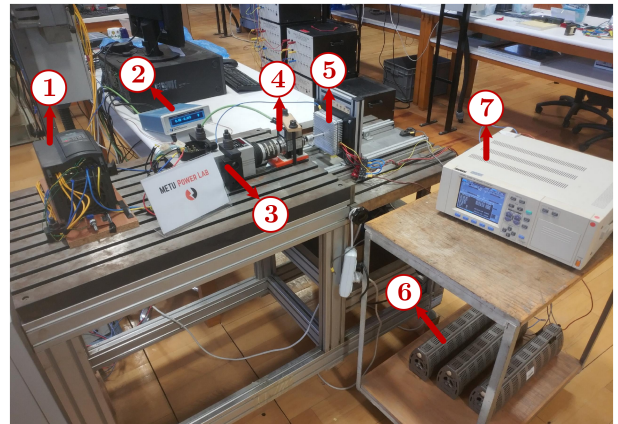


Fig. 18. Test setup for load tests. (1) Variable frequency drive, (2) Torque and speed display, (3) Induction machine, (4) Torque sensor, (5) PCB motor prototype, (6) Resistive load banks, (7) Three-phase power analyzer.

machine is directly proportional to the square of the width of the trace. As the average width of unequal width trace is 1.1 mm the eddy losses of the unequal width is much higher. The analytical calculation lacks the accuracy of FEA results however it is a good approach since eddy current analysis with 3D FEA is time consuming.

The results showed that although the resistance of the copper traces is lower, the unequal width winding cannot be effectively used in high-speed applications as it results in high amounts of eddy currents to be induced on wide copper traces. As presented in Fig. 6, eddy losses increase sharply as the copper trace width increases. However, it can be a good solution that does not have a high fundamental frequency since it has lower DC resistance compared to the constant width copper trace. The optimum trace width should be analyzed in each application to find the minimum amount of losses on stator windings.

C. Load Tests

A test setup is constructed to validate the operation of the prototype, as shown in Fig. 18. A three-phase induction machine has a maximum speed of 12000 RPM, and rated power of 1.5 kW is used to drive the PCB motor. Mechanical power is measured with the torque and speed readings of the sensor. The machine is loaded in generating mode of operation with a three-phase load bank, and a power analyzer is used to measure the output power.

The machine is loaded for three different power levels. The half load is at 6000 RPM and 2 A of current. The machine operated at 6000 RPM and 4 A current at the full load. Moreover, the machine is tested under overload condition at 7000 RPM and 5 A to check the limits of the thermal solution. Temperature sensors are placed on and inside of the housings. The resultant temperature change inside the housing is presented in Fig. 19. Inside of the housing reached 43 °C and the stator temperature has reached 47 °C at full load, which has a 23 W loss. The thermal camera view of the motor under full load is shown in Fig. 20. The test results can also be seen in Table IV.

The PCB motor is also driven by the integrated motor driver. The field-oriented control is implemented after calibrating the

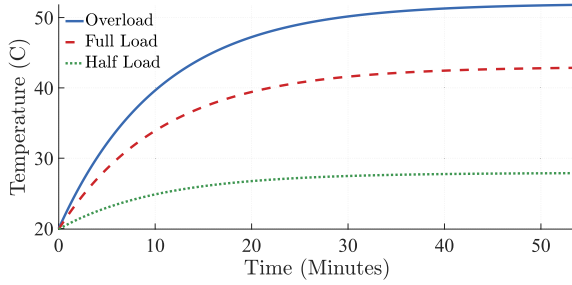


Fig. 19. Temperature change of the stator under overload, full load and half load.

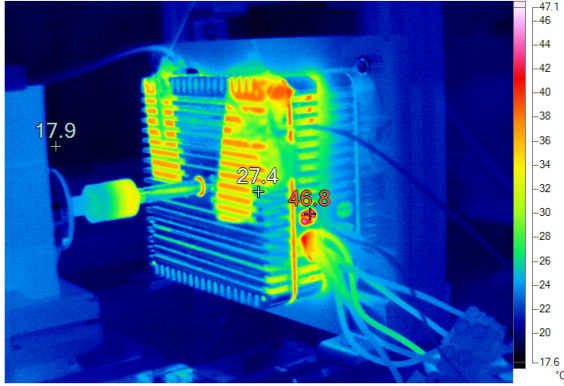


Fig. 20. Thermal camera view of the motor under full load test.

TABLE IV
TEST RESULTS OF THE MACHINE IN GENERATOR MODE

Test	Output power	Efficiency	Torque	Speed
Half load	102 W	90.1 %	0.18 N.m	6000 RPM
Full load	194 W	85.8 %	0.36 N.m	6000 RPM
Over load	270 W	81.5 %	0.45 N.m	7000 RPM

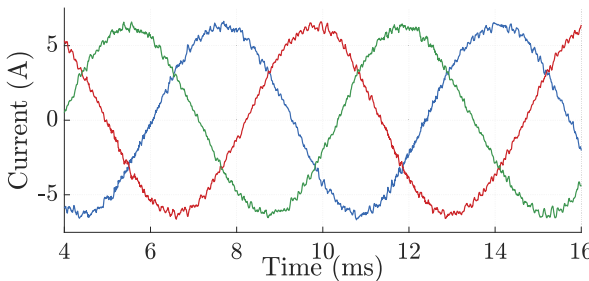


Fig. 21. Phase currents of the motor at rated torque.

encoder and the current measurements sensors. The current measurements are done at 100 kHz while the switching frequency is 1 MHz. Sinusoidal pulse width modulation is used to drive the motor up to 5000 RPM. The maximum speed of 6000 RPM can be reached using space-vector pulsed width modulation. The system is tested under two load torque conditions. The phase currents of the motor under 0.36 N.m load torque is presented in Fig. 21. The efficiency change of the overall integrated motor drive system is given in Fig. 22. The system showed 90% efficiency while under 0.18 N.m load torque at 5000 RPM. Under

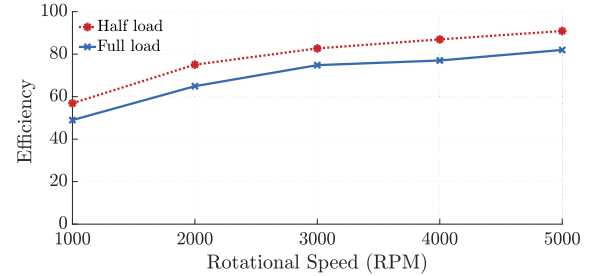


Fig. 22. Efficiency of the integrated motor drive system with respect to rotational speed at half and full load torque.

full load conditions, the system's overall efficiency is found as 82%.

III. CONCLUSION

An integrated motor drive with axial-flux permanent magnet synchronous machines with PCB stator is constructed for this paper. The developed analytical model is verified on FEA and with experimental results. Two stators are designed with unequal width winding and constant 0.35 mm width to observe the effect of eddy losses on PCB stators. The results showed that unequal width windings better suited for low fundamental frequency applications since the eddy currents are not dominant in this range. For higher fundamental frequency applications trace width should be decreased in order to limit eddy current losses. A GaNFET switched integrated motor driver is implemented and the motor is driven using field-oriented control at a switching frequency of 1 MHz. The mechanical and thermal design is proposed for double rotor single stator axial-flux permanent magnet machines using the PCB stator surface. The heat generated in the stator is transferred to the outer edges using the copper trace, and it is passively dissipated to the ambient. The cooling methodology used in this paper shows an efficient solution for both switches and microcontroller on driver circuitry and the double-sided axial-flux machine. The results showed that the stator temperature reached 47 °C at rated load using natural convection.

REFERENCES

- [1] S.. Neethu, S. P. Nikam, S. Pal, A. K. Wankhede, and B. G. Fernandes, "Performance comparison between PCB-stator and laminated-core-stator-based designs of axial flux permanent magnet motors for high-speed low-power applications," *IEEE Trans. Ind. Electron.*, vol. 67, no. 7, pp. 5269–5277, Jul. 2020.
- [2] R. Huang, Z. Song, H. Zhao, and C. Liu, "Overview of axial-flux machines and modeling methods," *IEEE Trans. Transport. Electric.*, vol. 8, no. 2, pp. 2118–2132, Jun. 2022.
- [3] O. Taqavi and S. M. Mirimani, "Design aspects, winding arrangements and applications of printed circuit board motors: A comprehensive review," *IET Electric Power Appl.*, vol. 14, no. 9, pp. 1505–1518, 2020.
- [4] F. Nishanth, J. V. Verdegem, and E. L. Severson, "Recent advances in analysis and design of axial-flux permanent-magnet electric machines," in *Proc. IEEE Energy Convers. Congr. Expo.*, 2021, pp. 3745–3752.
- [5] B. Anvari, P. Guedes-Pinto, and R. Lee, "Dual rotor axial-flux permanent-magnet motor using PCB stator," in *Proc. IEEE Int. Electric Mach. Drives Conf.*, 2021, pp. 1–7.

- [6] N. S., S. P. Nikam, S. Singh, S. Pal, A. K. Wankhede, and B. G. Fernandes, "High-speed coreless axial-flux permanent-magnet motor with printed circuit board winding," *IEEE Trans. Ind. Appl.*, vol. 55, no. 2, pp. 1954–1962, Mar./Apr. 2019.
- [7] F. Tokgöz, G. Çakal, and O. Keysan, "Comparison of PCB winding topologies for axialflux permanent-magnet synchronous machines," *IET Electric Power Appl.*, vol. 14, no. 13, pp. 2577–2586, 2020.
- [8] F. Tokgöz, "Analytical modelling and multi-objective optimization of axial-flux permanent-magnet machine with various PCB stators and development of a GAN switched integrated motor drive PCB motor," M.S. thesis, Graduate Sch. Natural Appl. Sci., Middle East Tech. Univ., Ankara, Turkey, 2022.
- [9] S. De, M. Rajne, S. Poosapati, C. Patel, and K. Gopakumar, "Low-inductance axial flux BLDC motor drive for more electric aircraft," *IET Power Electron.*, vol. 5, no. 1, 2012, Art. no. 124.
- [10] X. Zhang, N. Haryani, Z. Shen, R. Burgos, and D. Boroyevich, "Ultra-low inductance phase leg design for GAN-based three-phase motor drive systems," in *Proc. IEEE 3rd Workshop Wide Bandgap Power Devices Appl.*, 2015, pp. 119–124.
- [11] A. H. Mohamed, H. Vansompel, and P. Sergeant, "An integrated modular motor drive with shared cooling for axial flux motor drives," *IEEE Trans. Ind. Electron.*, vol. 68, no. 11, pp. 10467–10476, Nov. 2021.
- [12] M. Schiestl et al., "Development of a high power density drive system for unmanned aerial vehicles," *IEEE Trans. Power Electron.*, vol. 36, no. 3, pp. 3159–3171, Mar. 2021.
- [13] P. Han, G. Heins, Y. Zhang, and D. M. Ionel, "Integrated modular motor drives based on multiphase axial-flux PM machines with fractional-slot concentrated windings," in *Proc. IEEE Int. Electric Machines Drives Conf.*, 2021, pp. 1–6.
- [14] T. M. Jahns and B. Sarlioglu, "The incredible shrinking motor drive: Accelerating the transition to integrated motor drives," *IEEE Power Electron. Mag.*, vol. 7, no. 3, pp. 18–27, Sep. 2020.
- [15] A. Bauer, B. H. Zacher, and C. Schumann, "Enhanced cooling of multi-layer PCB motor windings using thermal vias," in *Proc. IEEE 47th Annu. Conf. Ind. Electron. Soc.*, 2021, pp. 1–5.
- [16] F. Tokgöz, O. Gülsuna, F. Karakaya, G. Çakal, and O. Keysan, "Design of an optimized PCB motor with a GAN switched integrated motor drive," in *Proc. 11th Int. Conf. Power Electron., Mach. Drives*, 2022, vol. 2022, pp. 429–433.
- [17] Z. Q. Zhu, D. Howe, E. Bolte, and B. Ackermann, "Instantaneous magnetic field distribution in brushless permanent magnet DC motors. I. Open-circuit field," *IEEE Trans. Magn.*, vol. 29, no. 1, pp. 124–135, Jan. 1993.
- [18] E. P. Furlani, "Computing the field in permanent-magnet axial-field motors," *IEEE Trans. Magn.*, vol. 30, no. 5, pp. 3660–3663, Sep. 1994.
- [19] T. F. Chan, L. L. Lai, and S. Xie, "Field computation for an axial flux permanent-magnet synchronous generator," *IEEE Trans. Energy Convers.*, vol. 24, no. 1, pp. 1–11, Mar. 2009.
- [20] F. Tokgöz, G. Çakal, and O. Keysan, "Design and implementation of an optimized printed circuit board axial-flux permanent-magnet machine," in *Proc. Int. Conf. Elect. Mach.*, vol. 1, 2020, pp. 111–116.
- [21] K. Deb, A. Pratap, S. Agarwal, and T. Meyarivan, "A fast and elitist multiobjective genetic algorithm: NSGA-II," *IEEE Trans. Evol. Comput.*, vol. 6, no. 2, pp. 182–197, Apr. 2002.
- [22] L. A. Pereira, S. Haffner, G. Nicol, and T. F. Dias, "Multiobjective optimization of five-phase induction machines based on NSGA-II," *IEEE Trans. Ind. Electron.*, vol. 64, no. 12, pp. 9844–9853, Dec. 2017.
- [23] A. K. Morya et al., "Wide bandgap devices in AC electric drives: Opportunities and challenges," *IEEE Trans. Transport. Electricific.*, vol. 5, no. 1, pp. 3–20, Mar. 2019.
- [24] T. Jahns, "Getting rare-earth magnets out of EV traction machines: A review of the many approaches being pursued to minimize or eliminate rare-earth magnets from future EV drivetrains," *IEEE Electricific. Mag.*, vol. 5, no. 1, pp. 6–18, Mar. 2017.



Furkan Tokgoz (Student Member, IEEE) received the B.Sc. and M.Sc. degrees in electrical-electronics engineering from Middle East Technical University, Ankara, Turkey, in 2019 and 2022, respectively. He is currently working toward the Ph.D. degree with the University of Sheffield, Sheffield, U.K., as a Member of Electrical Machines and Drives Group. His research interests include less rare-earth permanent magnet machines for electric vehicles, integrated motor drive axial-flux machines, and PCB stators.



Özgür Gülsuna is currently working toward the B.Sc. degree from the Department of Electrical and Electronics Engineering, Middle East Technical University, Ankara, Turkey. His research interests include capture data driven design, reliability and durability in power electronics, and wide bandgap devices.



electrical motor drivers.



facturing technology.

Furkan Karakaya (Student Member, IEEE) received the B.Eng. and M.Sc. degrees in electrical and electronics engineering from Middle East Technical University, Ankara, Turkey, in 2017 and 2020, respectively. He is currently working toward the Ph.D. degree with the University of Illinois Urbana-Champaign, Champaign, IL, USA, as a Member of the Power Energy Systems Research Group. His research interests include power electronics, device characterization, applications and reliability of wide bandgap transistors, and integrated and fault-tolerant

Gokhan Cakal (Student Member, IEEE) received the B.S. and M.S. degrees in electrical engineering from Middle East Technical University, Ankara, Turkey, in 2017 and 2020, respectively. He is currently working toward the Ph.D. degree in electrical and computer engineering with the University of Wisconsin-Madison, Madison, WI, USA. He has been a Research Assistant with the Wisconsin Electric Machines and Power Electronics Consortium, Madison, WI, USA, since 2021. His research focuses on innovative cooling solutions for electric machines with additive manu-



Ozan Keysan (Member, IEEE) received the B.Sc. and M.Sc. degrees from Middle East Technical University (METU), Ankara, Turkey, in 2005 and 2008, respectively, and the Ph.D. degree from the University of Edinburgh, Edinburgh, U.K., in 2014. He is currently an Assistant Professor with the Department of Electrical and Electronics Engineering, METU. His research interests include renewable energy, design and optimization of electrical machines, smart grids, superconducting machines, and permanent-magnet machines.